Experimental and computational validation and verification of the coupled continuum pipe-flow and Stokes-Darcy models for karst aquifers

Fei Hua,[1] Max Gunzburger,[2] Bill X. Hu,[3] Xiaoming Wang,[4] Yanzhao Cao[5]

Corresponding author:

Bill X. Hu

Department of Geological Sciences

Florida State University

Tallahassee, Florida, USA

hu@gly.fsu.edu

Telephone: 850-644-3743

Keywords:

karst aquifers; conduit and matrix domains; pipe-flow model;

Stokes-Darcy model; Beavers-Joseph interface condition

[1]Courant Institute of Mathematical Sciences, New York University, New York, New York, USA

[2]Department of Scientific Computing, Florida State University, Tallahassee, Florida, USA

[3]Department of Geological Sciences, Florida State University, Tallahassee, Florida, USA.

[4]Department of Mathematics, Florida State University, Tallahassee, Florida, USA

[5]Department of Mathematics, Auburn University, Auburn, Alabama, USA

Abstract.

The coupled continuum pipe-flow (CCPF) and Stokes-Darcy (SD) models for flows in conduit/matrix systems are reviewed as are mathematical results about the well-posedness of the models. In particular, for the SD model, we review the use of asymptotic solutions in a validation study of the four choices used in the literature for the matrix/conduit interface conditions, concluding that the Beavers-Joseph (BJ) interface condition is the most accurate. Then, we review the use of numerical analyses to validate finite element discretization methods for the two models. Using computational experiments, simulation codes implementing the finite element discretizations are then verified. Further model validation studies are based on the results of laboratory experiments whose setup we describe. Comparing the results of computer simulations and experiments, we conclude that the SD model with the BJ interface condition is a valid model for conduit/matrix systems. On the other hand, the CCPF model with the value of the exchange parameter chosen within the range suggested in the literature perhaps does not result in good agreement with experimental observations. We then examine the sensitivity of the CCPF model with respect to the exchange parameter, concluding that, as has previously been noted, the model is highly sensitive for small values of the exchange parameter. However, for larger values, the model becomes less sensitive and, more important, also produces results that are in better agreement with experimental observations. This suggests that the CCPF model

may also produce accurate simulation results, if one chooses larger values of the exchange parameter than those suggested in the literature.

1. Introduction

Karst aquifers are susceptible to greater contamination than are non-karstic aquifers due to rapid transport processes and limited chemical filtering capacities, both of which quicken the spread of solutes *Taylor et al.* [2001]; *Matusick et al.* [2007]; *Kuniansky* [2008]. In comparison with the large amount of quantitative studies of groundwater flow and contaminant migration in porous and fractured media, similar studies in karst aquifers are very limited and inaccurate, despite the fact that, in many states, karst aquifers represent a very significant source of water for public and private use *Kincaid* [2004]. A karst aquifer, in addition to a porous limestone matrix, typically has large cavernous conduits that are known to largely control groundwater flow and contaminant transport within the aquifer *Katz et al.* [1998]. During a high-flow season, the water pressure in the conduits is larger than that in the ambient matrix so that conduit-borne contaminants can be driven into the matrix. During dry seasons, the pressure differential reverses and contaminants long sequestered in the matrix can be released into the free flow in the conduits and exit through, e.g., springs and wells, into surface water systems *Li et al.* [2008]. This retention and release phenomenon induces an environmental issue in that sequestered contaminants may influence the quality of underground water sources for a long time and thus significantly decrease water availability. Figure 1 provides a sketch of the conceptual model of a karst aquifer. In that figure, Ω_m and Ω_c denote the matrix and conduit domains, respectively, Γ_g the ground surface, Γ_{si} and Γ_{sp} a sinkhole and spring boundary, respectively, Γ_{cm} the conduit/matrix interface boundary, and Γ_0 a bounding surface that is presumably far removed from the region of interest.

The dual character of a karst flow system is widely recognized and stems from the existence of different porosities within a karst aquifer *Ford* [1998]; *Worthington* [2003] which determine the type of flow prevailing in the aquifer *Ford et al.* [1989]; *Bauer et al.* [2003]. Similar to the dual-porosity/permeability model widely used for fractured media *Gerke et al.* [1993a, b], the coupled continuum pipe-flow (CCPF) model has been proposed to describe the flow and solute transport in karst aquifers *MacQuarrie et al.* [1996]; *Chen et al.* [1988]; *Kiraly* [1998]; *Bauer et al.* [2000, 2003]; *Birk et al.* [2003]. The CCPF model is a dual flow system system consisting of a matrix representing the bulk mass of permeable limestone and a conduit system representing the karst conduit network. Flow exchange between the two systems is controlled by differences in hydraulic heads as well as the hydraulic conductivity and the geometric setting. In the CCPF model, the groundwater flow in the matrix is described by the Darcy's law and the flow in the conduit is modeled by a pipe-flow model. The water mass exchange flow rate between the two systems q_{ex} is described by a first-order mass exchange model; the exchange flow rate is assumed to be linearly proportional to the head difference between the two systems *Barenblatt et al.* [1960]; *Cao et al.* [1988]; *Teutsch* [1989]; *Sauter* [1992]. The exchange rate coefficient is a lumped parameter and its value will depend on many factors including, among others, the hydraulic conductivity in the matrix, the exchange surface between the conduit and matrix, and conduit geometry *Barenblatt et al.* [1960]; *Liedl et al.* [2003]. The value of the exchange rate parameter is not usually obtained from measurements but rather through curve-fitting. Based on the CCPF model, a new numerical method has been developed and became part of the new MODFLOW software *Shoemaker et al.* [2008]. However, the suitability and validity of the CCPF model as a model for groundwater flow in a karst

aquifer, especially for the flow exchange between matrix and conduits, has not been well studied. In addition, the determination of the value of the exchange rate parameter is also an issue that needs attention.

Flow in karst aquifers, and especially the exchange of water and contaminants between the matrix and the conduits, can also be modeled by coupling the Darcy model for the flow in the matrix with the Navier-Stokes equations (or Stokes under low Raynolds number assumption) for the flow in the conduits. In this case, we have three-dimensional conduits (in constrast to the one-dimensional conduits of the pipe-flow model) embedded in the matrix and the exchange of water and water-borne contaminants occurs at the boundaries between the matrix and conduits. In *Beavers et al.* [1967], interface conditions, referred to as the Beavers-Joseph conditions, governing that exchange were developed based on experimental observations; these have become widely accepted. However, the Beavers-Joseph conditions engender mathematical and computational difficulties so that several simplifications have been proposed *Saffman* [1971]; *Jones* [1973]; *Discacciati et al.* [2002]. Recently, in the setting of Stokes system for the flow in the conduits, the Beavers-Joseph conditions have been studied from the mathematical and computational viewpoints *Cao et al.* [2009a, b, c]; *Chen et al.* [2009]. Furthermore, computational results for the coupled SD model have been compared to results obtained from laboratory experiments *Faulkner et al.* [2009].

The purpose of this study is to use mathematical, computational, and experimental means for the verification and validation of the CCPF and SD models and of finite element discretization algorithms and their implementations. Obtaining information about good

choices for the values of the exchange parameters appearing in the models is also an objective of this study.

In Section 2, we provide descriptions of the CCPF and SD models and briefly touch on the mathematical issues of well-posedness of the models and on mathematical and computational results obtained from finite element discretizations. For the SD model, the results of asymptotic comparisons of the SD models with the Beavers-Joseph condition and three simplifications of that condition are provided, using the more sophisticated Stokes-Brinkman model as a benchmark. In Section 3, we compare results obtained from the two models to results obtained from laboratory experiments. We describe the laboratory setup and provide the comparisons between experiments and simulations. In Section 4, we use results obtained with the CCPF model to study the sensitivity of that model with respect to a modeling parameter (the exchange rate coefficient) and, using the validated SD model as a benchmark, glean some insight as to effective choices for the value of that parameter. Finally, in Section 5, we provide some concluding remarks.

2. Models for Matrix/Conduit Flows

In this section, we consider two models for determining flow velocities and pressures in karst-like systems consisting of a porous matrix in which conduits are embedded. For both models, the Darcy equation is used for the flow in the matrix; for the free flow in the conduits, one uses a one-dimensional pipe-flow model whereas the other uses the Stokes equations. An particularly important aspect we address is the proper accounting of the fluid exchange between the matrix and the conduit.

The velocity field in the matrix $\mathbf{v}_m$ determined from the either the coupled pipe-flow-Darcy or coupled SD systems is used in the governing equation for the tracer evolution in the matrix

$$\frac{\partial C_m}{\partial t} + \mathbf{v}_m \cdot \nabla C_m - \nabla \cdot (D_m \nabla C_m) = F_m, \tag{1}$$

where C_m denotes the solute concentration in the matrix, D_m the dispersion coefficient, and F_m solute sources and sinks. Ideally, one should couple the tracer density in the matrix and conduit. However, assuming that the flow in the channel moves significantly faster than that in the matrix, we simply impose a Dirichlet boundary condition for C_m along the matrix/conduit interface and a homogeneous Neumann boundary condition elsewhere on the matrix boundary.

2.1. The Coupled Continuum Pipe-Flow Model

2.1.1. CCPF model formulation

We denote by Ω_m the domain occupied by the porous media and by Ω_p the one-dimensional (possibly) curved pipes that we use as surrogates for the embedded conduits. Although the conduits are modeled by one-dimensinal curves, the do come imbued with a diameter parameter d. For the coupled continuum pipe flow (CCPF) model, the conceptual model sketched in Figure 1 reduces to that in Figure 2.

The flow in the porous matrix is modeled by a continuum approach using the Boussinesq equation *Bear et al.* [1987]

$$S\frac{\partial h_m}{\partial t} - \nabla \cdot (K \nabla h_m) = \gamma + f_m \qquad \text{in } \Omega_m, \tag{2}$$

where $K(x, y, z) > 0$ denotes the hydraulic conductivity, S the storativity, γ the volumetric rate per unit length of fluid transfered to the porous matrix system from the conduit system, f_m the flow rate of the fluid entering or exiting the matrix through sources and sinks, and h_m denotes the hydraulic (piezometric) head defined as $h_m = z + \frac{p_m}{\rho g}$, where p_m denotes the dynamic pressure, z the height, ρ the density, and g the gravitational constant.

For the conduit flow, i.e., the flow along the pipes Ω_p, the discharge can be related to the head difference in the tube by applying the Darcy-Weisbach equation *Bobok* [1993]

$$\frac{\partial h_p}{\partial \tau} = -\lambda \frac{u|u|}{2dg} \qquad \text{along } \Omega_p, \tag{3}$$

where τ denotes the tangential direction along the one-dimensional pipe conduit, $u = 4Q/(\pi d^2)$ the average velocity, g the gravitational acceleration, and Q the total discharge in the pipe. The friction factor λ depends on the velocity in the pipe via the Reynolds number $Re = |u|d/\nu$, with ν the kinematic viscosity of water. For low flow velocities, laminar flow is assumed and the Hagen-Poiseuille equation can be applied for the flow in the conduit. The friction factor for laminar flow is calculated as $\lambda = 64\nu/(d|u|)$. Substituting these definitions into (3), we obtain $Q = -D\partial h_p/\partial \tau$, where $D = \pi d^4 g/128\nu$. Conservation of mass in the pipe implies that $\partial Q/\partial \tau = -\gamma$. Hence, we have

$$-\frac{\partial}{\partial \tau}\Big(D\frac{\partial h_p}{\partial \tau}\Big) = -\gamma \delta_{\Omega_p} + f_p \qquad \text{along } \Omega_p, \tag{4}$$

where δ_{Ω_p} represents the Dirac δ function concentrated on Ω_p; in practice, $f_p = 0$ but is included here to facilitate the study of the convergence behavior of finite element discretiza-

tions. We remark that the formulas given for u, λ, and D are for the three-dimensional case; in two dimensions, these change to $u = Q/d$, $\lambda = 24\nu/(d|u|)$, and $D = d^3 g/(12\nu)$.

The matrix and conduit flows are coupled through the exchange term γ which is given by *Barenblatt et al.* [1960]; *Narasimhan* [1982]

$$\gamma = \alpha_{ccpf}(h_p - h_m), \tag{5}$$

where $\alpha_{ccpf} > 0$ denotes the *exchange rate coefficient.* We can interpret (5) as saying that the flow process in the conduit is slaved to that in the fissured matrix. We remark that the exchange rate coefficient is the key parameter into which, unfortunately, most of the uncertainties are lumped so that it may be viewed as a tuning parameter for the CCPF model.

Collecting (2), (4), and (5), we have that

$$\begin{cases} S\dfrac{\partial h_m}{\partial t} - \nabla\cdot(K\nabla h_m) \\ \qquad\qquad = -\alpha_{ccpf}(h_m - h_p)\delta_{\Omega_p} + f_m \ \text{ in } \Omega_m \\ -\dfrac{\partial}{\partial\tau}\Big(D\dfrac{\partial h_p}{\partial\tau}\Big) = \alpha_{ccpf}(h_m - h_p) + f_p \quad \text{along } \Omega_p. \end{cases} \tag{6}$$

This coupled system is supplemented by initial and boundary conditions. For example, at the end points of the conduit (Γ_{si} and Γ_{sp} in Figure 2), h_p is specified; on the boundary of the matrix we have h_m specified along Γ_g and $K\nabla h_m \cdot \mathbf{n} = 0$ along Γ_0.

In this paper, we consider a simplified, *steady-state, two-dimensional* setting. The following geometrical setup is used. The matrix continuum is assumed to occupy the square $\Omega_m = \{0 < x < 1\,,\, -1/2 < y < 1/2\}$ and the one-dimensional conduit pipe lies in the middle so that $\Omega_p = \{0 < x < 1\,,\, y = 0\}$. Then, (6) reduces to

$$\begin{cases} -\nabla \cdot (K\nabla h_m) = \\ \qquad -\alpha_{ccpf}(h_m(x,0) - h_p(x))\delta(y) + f_m \ \text{ in } \Omega_m \\ -\dfrac{d}{dx}(D\dfrac{dh_p}{dx}) = \alpha_{ccpf}(h_m|_{y=0} - h_p) + f_p \ \text{ in } \Omega_p, \end{cases} \tag{7}$$

where $\delta(y)$ denotes the Dirac delta function in y. In addition, we impose the fixed-head (Dirichlet) boundary conditions for the purpose of numerical analysis

$$\begin{cases} h_m = g_m \quad \text{on } \partial\Omega_m = \text{boundary of } \Omega_m, \\ h_p = g_{c0} \quad \text{at } x = 0, \qquad h_p = g_{c1} \quad \text{at } x = 1, \end{cases} \tag{8}$$

where g_m is a given function and g_{c0} and g_{c1} are given numbers. In simulations, fixed-flow-rate (Neumann) boundary condition can be applied to the ends of the conduit as well.

In *Cao et al.* [2009c], it is proved that, in the *steady-state* case, the two-dimensional problem (7)–(8) is well posed, i.e., a unique solution exists and, in appropriate norms, depends continuously on the data, i.e., the forcing terms f_m and f_p. Additional regularity of the solution is also proved in case the given data is smoother than that required for the existence of the solution.

2.1.2. Verification of finite element discretizations of the CCPF model

In *Cao et al.* [2009c], finite element methods for the discretization of (7)–(8) are developed and analyzed. The well-posedness of the discrete problem obtained from the finite element discretization is proved and error estimates are derived for the cases of continuous piecewise linear and quadratic finite element functions. In particular, it is shown that if the exact solution of (7)–(8) is sufficiently smooth and the conduit pipe Ω_p does not intersect with the interior of any finite element, then, for arbitrary $0 < \epsilon < \frac{1}{2}$,

$$\begin{aligned} |h_m - h_m^{fe}|_{\Omega_m,1} + |h_p - h_p^{fe}|_{\Omega_p,1} &\le Ch^k \\ \|h_m - h_m^{fe}\|_{\Omega_m,0} + \|h_p - h_p^{fe}\|_{\Omega_p,0} &\le Ch^{k+\frac{1}{2}-\epsilon}, \end{aligned} \tag{9}$$

where h_m^{fe} and h_p^{fe} denote the finite element approximations of h_m and h_p, respectively, h a measure of the grid size, k the degree of the polynomials used ($k = 1$ for piecewise linear case and $k = 2$ for the piecewise quadratic case), and C a generic constant whose value is independent of h. In (9), the L^2 norms $\|\cdot\|_{\Omega_m,0}$ and $\|\cdot\|_{\Omega_p,0}$ and the H^1 semi-norms $|\cdot|_{\Omega_m,1}$ and $|\cdot|_{\Omega_p,1}$ are defined by

$$\begin{aligned} \|h_m\|^2_{\Omega_m,0} &= \int_{\Omega_m} h_m^2 \, dxdy, \\ |h_m|^2_{\Omega_m,1} &= \int_{\Omega_m} |\nabla h_m|^2 \, dxdy, \\ \|h_p\|^2_{\Omega_p,0} &= \int_0^1 h_p^2 \, dx, \\ |h_p|^2_{\Omega_p,1} &= \int_0^1 \Big|\frac{dh_p}{dx}\Big|^2 \, dx. \end{aligned}$$

It is also shown in *Cao et al.* [2009c] that if K is constant, then for the piecewise linear case we have the optimal estimate

$$\|h_m - h_m^{fe}\|_{\Omega_m,0} + \|h_p - h_p^{fe}\|_{\Omega_p,0} \le Ch^2. \tag{10}$$

If the conduit pipe Ω_p does intersect with the interiors of the finite elements, then the exponents of h in the error estimates in (9) reduce to $\frac{1}{2} - \epsilon$ and $1 - 2\epsilon$, respectively.

We use the method of manufactured solutions to verify the finite element code we developed for the approximate solution of (7)–(8). All parameters, including the hydraulic conductivity and exchange rate, are set to unity and the forcing functions f_m and f_c are determined from the exact solution

$$\begin{cases} h_p = 2\sin(2\pi x) & \text{in } \Omega_p, \\ h_m = \sin(2\pi x) & \text{in } (0,1)\times(-1/2,0] \subset \Omega_m, \\ h_m = (-\frac{\alpha_{ccpf}}{K} y + 1)\sin(2\pi x) & \\ & \text{in } (0,1)\times[0,1/2) \subset \Omega_m. \end{cases}$$

For this exact solution, we are in a situation where (9) and (10) apply. Computational results are obtained for continuous piecewise linear and piecewise quadratic finite element spaces based on uniform grids. The errors obtained and the estimated convergence rates are summarized in Tables 1 and 2.

For the piecewise linear case ($k = 1$), the second-order convergence rates for the L^2 norm of the errors and the first-order convergence rates for the H^1 semi-norm of the errors shown in Table 1 completely agree with the analyses given in *Cao et al.* [2009c]; see (10) and the first estimate in (9). For the piecewise quadratic case ($k = 2$), the second-order convergences rates for the H^1 semi-norm of the errors shown in Table 2 agree with the analyses of *Cao et al.* [2009c]; see (9). The third-order convergences rates for the L^2 norm of the errors shown in Table 2 are better that those predicted by (9); this improved computational result may be due to the high smoothness of the exact solution we are dealing with and many not hold for general solutions of (7)–(8).

In summary, through the error estimates in (9), we have analytically verified the accuracy of the finite element discretization of (7)–(8), i.e., we have shown that the finite element methods provide accurate approximations of exact solutions. Through the computational experiments reported in Tables 1 and 2 as well as others, we have computationally verified the finite element codes we have developed, i.e., the code correctly computes the finite element approximations.

We remark that the mathematical and numerical results reviewed here for the CCPF model also hold in the *three-dimensional* case of a porous matrix coupled with a *two-dimensional* conduit, i.e., the conduit is a surface in three dimensions. The proof of well-posedness remains the same, whereas the regularity and numerical analysis can be treated in a very similar fashion. For the coupling of a three-dimensional porous matrix with a *one-dimensional* conduit, the rigorous mathematical treatment is not straightforward because the coupling introduces a strongly singular forcing term to the Darcy equation. Despite the lack of mathematical rigor, such three-dimensional/one-dimensional couplings are used, at the discrete level, in practice.

2.2. The SD Model

2.2.1. SD model formulation

We next consider Stokes-Darcy (SD) models for coupled conduit/matrix flows. We refer to Figure 1 for geometric notation. The flow in the porous matrix is again governed by

$$S\frac{\partial h_m}{\partial t} + \nabla \cdot (-K\nabla h_m) = f_m \quad \text{in } \Omega_m. \tag{11}$$

Comparing with (2), we see that the exchange term γ is not present; this is because the exchange of fluid between the matrix and conduit is now modeled by interface conditions at the boundary between the matrix and the conduit, both of which now have finite volume. The exchange term γ was needed in (2) because the conduit in that case has zero volume so interface "boundary" conditions are not applicable.

We impose the boundary conditions

$$h_m = 0 \quad \text{on } \Gamma_g, \qquad K\nabla h_m \cdot \mathbf{n} = 0 \quad \text{on } \Gamma_0, \tag{12}$$

along the boundary of the matrix, the first of which naturally implies that the hydraulic head is zero at the ground surface if the matrix is saturated and the second, is a reasonable fictitious boundary condition useful for analysis and simulation purposes.

In the conduit Ω_c, the Navier-Stokes equations

$$\begin{cases} \dfrac{\partial \mathbf{v}_c}{\partial t} + (\mathbf{v}_c \cdot \nabla)\mathbf{v}_c \\ \qquad = \nabla \cdot (-p_c I + 2\nu D(\mathbf{v}_c)) - g\mathbf{k} & \text{in } \Omega_c \\ \nabla \cdot \mathbf{v}_c = 0 & \text{in } \Omega_c \end{cases} \tag{13}$$

govern the free flow. Here, $\mathbf{v}_c$ denotes the flow velocity in the conduit, p_c the kinematic pressure, $D(\mathbf{v}) = \frac{1}{2}(\nabla\mathbf{v} + (\nabla\mathbf{v})^T)$ the rate of deformation tensor, ν the kinematic viscosity, and $\mathbf{k}$ the unit vector in the z direction. In this paper, we assume that the value of the Reynolds number is small so that we are able to replace the Navier-Stokes system by the linear Stokes system

$$\begin{cases} \dfrac{\partial \mathbf{v}_c}{\partial t} = \nabla \cdot (-p_c I + 2\nu D(\mathbf{v}_c)) - g\mathbf{k} & \text{in } \Omega_c \\ \nabla \cdot \mathbf{v}_c = 0 & \text{in } \Omega_c. \end{cases} \tag{14}$$

At the sinkhole and the spring, we respectively specify the inflow and outflow velocities:

$$\begin{cases} \mathbf{v}_c \times \mathbf{n} = \mathbf{0}, \quad \mathbf{v}_c \cdot \mathbf{n} = \gamma_{si}(t)\eta_{si}(\mathbf{x}) = f_{si} & \text{on } \Gamma_{si} \\ \mathbf{v}_c \times \mathbf{n} = \mathbf{0}, \quad \mathbf{v}_c \cdot \mathbf{n} = \gamma_{sp}(t)\eta_{sp}(\mathbf{x}) = f_{sp} & \text{on } \Gamma_{sp}, \end{cases} \tag{15}$$

where γ, η, and f are given functions defined at the spring and the sinkhole, and $\mathbf{n}$ is the unit outer normal to Γ_{si} and Γ_{sp}. These boundary conditions are usually what is measured

in the field or in the lab. The time dependence built into the data in (15) allows one to model flood and drought seasons.

In addition to the boundary conditions (12) and (15) imposed along the boundary of the matrix and conduit, respectively, we apply the following interface boundary conditions that couple the solutions in the two domains:

$$\begin{cases} \mathbf{v}_c \cdot \mathbf{n}_{cm} = \mathbf{v}_m \cdot \mathbf{n}_{cm} & \text{on } \Gamma_{cm} \\ -\mathbf{n}_{cm}^T T(\mathbf{v}_c, p_c)\mathbf{n}_{cm} = g(h_m - z) & \text{on } \Gamma_{cm} \\ -\boldsymbol{\tau}_i^T D(\mathbf{v}_c)\mathbf{n}_{cm} = & \\ \quad \dfrac{\alpha_{sd}\nu\sqrt{3}}{\sqrt{\text{trace}(\Pi)}}\boldsymbol{\tau}_i^T(\mathbf{v}_c - \mathbf{v}_m), \;\; i = 1, 2, & \text{on } \Gamma_{cm}, \end{cases} \tag{16}$$

where $\{\boldsymbol{\tau}_1, \boldsymbol{\tau}_2\}$ represents a local orthonormal basis for the tangent plane to Γ_{cm}, $\mathbf{n}_{cm}$ denotes the unit normal to Γ_{cm} pointing from the conduit to the matrix, $T(\mathbf{v}_c, p_c) := -p_c I + 2\nu D(\mathbf{v}_c)$ the stress tensor, $\mathbf{v}_m$ the flow velocity obtained by relation $\mathbf{v}_m = -K\nabla h_m$, $\Pi = \mu K/(\rho g)$ the intrinsic permeability and α_{sd} a constant parameter that presumably depends on the properties of the porous material as well as the geometrical setting of the coupled problem and that can be used to tune the model.

The first two interface conditions in (16) are quite natural. The first guarantees the conservation of mass, i.e., the exchange of fluid between the two domains is conservative. The second condition is a balance of the normal components of the stress force along the interface Γ_{cm} which in the present case balances the kinematic pressure of the flow in the matrix and the normal component of the stress force in the free flow in the conduit. The last equation in (16) is the *Beavers-Joseph* condition *Beavers et al.* [1967] that is generally accepted as a good model for how the porous media affects the conduit flow at the interface. This condition was derived based on empirical observations and states that

the tangential component of stress force on the conduit side of the interface is proportional to the jump in the tangential velocity across the interface.

Several simplifications of the Beavers-Joseph interface conditions have been proposed and are in use. In *Saffman* [1971] (see also *Jones* [1973]), asymptotic analyses is used to show, under several hypotheses, that as the hydraulic conductivity in the porous medium tends to zero, the flow velocity on the matrix side of the interface is of higher order compared to that on the conduit side. Thus, the term $\{\boldsymbol{\tau}_i^T(\mathbf{v}_m)$ that involves the tangential component of the velocity in the matrix is omitted from the right-hand side of the Beavers-Joseph condition, resulting in the *Beavers-Joseph-Saffman-Jones* condition

$$-\boldsymbol{\tau}_i^T D(\mathbf{v}_c)\mathbf{n}_{cm} = \frac{\alpha_{sd}\nu\sqrt{3}}{\sqrt{\text{trace}(\Pi)}}\boldsymbol{\tau}_i^T\mathbf{v}_c, \quad i = 1, 2, \quad \text{on } \Gamma_{cm}.$$

This simplification is also justified, under additional assumptions, in a more mathematically rigorous way in *Jäger et al.* [2000]. Numerical methods and analyses using the Beavers-Joseph-Saffman-Jones condition are given in, e.g., *Layton et al.* [2003]. Further simplifications of the Beavers-Joseph condition were used in *Discacciati et al.* [2002], where the whole right-hand side of the Beavers-Joseph interface boundary condition is omitted, i.e., a free slip boundary condition is applied, and in *Discacciati et al.* [2003, 2004]; *Jiang* [2009], where the whole left-hand side of the Beavers-Joseph-Saffman-Jones is omitted, i.e., the tangential velocity on the conduit side of the interface is set to zero.

2.2.2. Asymptotic analyses and validation studies of interface conditions for the SD model

We have just listed four interface conditions (Beavers-Joseph, Beavers-Joseph-Saffman-Jones, zero tangential conduit velocity, free slip) that are used in the literature when

coupling the Stokes (or Navier-Stokes) system for flow in the conduit to the Darcy system for flow in the matrix. Naturally, one wants to know something about the validity of the four choices, if only to justify the use of a particular choice. This is an important issue, given that the Beavers-Joseph interface condition leads to mathematical and computational difficulties that are greatly ameliorated by instead invoking any of other three simpler conditions.

Of course, we need a model to serve as the "truth" for the comparisons of the four interface conditions. For this purpose, we replace the Darcy model for the matrix flow with the Brinkman model, i.e., we couple the Stokes system (14) in the conduit to the Brinkman system *Brinkman* [1947]; *Neale et al.* [1974]; *Ochoa-Tapia et al.* [1995]; *Le Bars et al.* [2006] in the matrix, i.e., in the steady state, we have

$$\begin{cases} -2\nu\nabla\cdot D(\mathbf{v}_m) + \dfrac{\nu n}{\Pi}\mathbf{v}_m + n\nabla p_m = \vec{f}_m & \text{in } \Omega_m \\ \nabla\cdot\mathbf{v}_m = 0 & \text{in } \Omega_m \end{cases} \tag{17}$$

instead of the steady state version of (2). In (17), $\mathbf{v}_m$ denotes the flow velocity in the matrix, n the porosity and Π the permeability. The relationship between the porosity and permeability is given by $\Pi = \Pi_0 n^3/(1-n)^2$, where Π_0 is the typical permeability; see, e.g., *McCabe et al.* [2005]. It is well known that as the Darcy number $Da = \Pi_0/L^2$ (where L is a typical length scale in the matrix domain) goes to zero, the Brinkman system reduces to the Darcy equation (2) so that the latter may be viewed as a simplification of the former. In *Ochoa-Tapia et al.* [1995]; *Le Bars et al.* [2006], extensive discussions of interface conditions for coupling the Stokes and Brinkman systems are provided.

In *Chen et al.* [2009], simple model problems are used to obtain analytic solutions in one and two dimensions of the SD system with each of the four interface conditions and

for the Stokes-Brinkman system. Assuming $\epsilon = \sqrt{Da} \ll 1$, the leading order term for all five solutions are then obtained and compared. A summary of the results is given in Table 3. The column headings refer to the differences between the Stokes-Brinkman solutions and the SD solutions with Beavers-Joseph (BJ), Beavers-Joseph-Saffman-Jones (BJSJ), zero tangential conduit velocity (ZTCV), and free-slip (FS) interface conditions. The entries apply to both one- and two-dimensional solutions, although we have not verified the entries for the free-slip condition in two dimension due to its poor performance in one dimension.

From Table 3, we see that all four interface conditions for the SD system yield the same accuracy for the velocity in the matrix, when compared to the Stokes-Brinkman system. However, for the velocity in the conduit, we see that the Beavers-Joseph condition yields the best results, followed in order by the Beavers-Joseph-Saffman-Jones, the zero tangential conduit velocity, and the free-slip interface conditions. Certainly, the Beavers-Joseph condition is validated through these comparisons to the Stokes-Brinkman system.

2.2.3. Verification of finite element discretizations of the SD model

In our mathematical and computational studies, we do not invoke any of the simplified interface conditions and use the full form of the Beavers-Joseph condition included in (16). The well-posedness of the coupled SD model with the Beavers-Joseph interface condition was considered in *Cao et al.* [2009a]; *Hua* [2009]. In the steady-state case, well posedness is established under the assumption that the parameter α_{sd} in the Beavers-Joseph condition is small. In the time-dependent case, well posedness is established, under the assumption that the matrix media is isotropic, for general α_{sd} via an appropriate time discretization of the problem and a novel scaling of the system.

The convergence and error estimates for finite element approximations of the coupled SD systems with the Beavers-Joseph interface condition were obtained in *Cao et al.* [2009b]; *Hua* [2009].

For the computational experiments, we set $\Omega_m = (0,1) \times (0, 0.75)$ and $\Omega_c = (0,1) \times (-0.25, 0)$ so that the interface Γ_{cm} is given by $(0,1) \times \{0\}$. For simplicity, all the parameters appearing in (11), (14), and (16), i.e., the SD model with the Beavers-Joseph boundary condition, are set to unity and Dirichlet boundary conditions for $\mathbf{v}_c$ and h_m are applied on the boundary. The finite element spaces are defined with respect to a uniform grid. The Taylor-Hood element pair, i.e., continuous piecewise quadratic polynomials for the velocity components and continuous piecewise linear polynomials for the pressure, is used for the spatial discretization of the Stokes system. The Darcy system is discretized using continuous piecewise quadratic polynomials. The backward-Euler method with a constant time step is used to effect temporal discretization. In *Cao et al.* [2009b]; *Hua* [2009], error estimates are derived for this discretization scheme; a typical result is that, for sufficiently smooth exact solutions,

$$\|\mathbf{v}_c - \mathbf{v}_c^{fe}\|_0 + \|h_m - h_m^{fe}\|_0 \leq C(h^3 + \Delta t) \tag{18}$$

for a constant C whose value does not depend on the spatial grid size h or the time step Δt; in (18), $(\cdot)^{fe}$ denotes the finite element solution. Error estimates for the steady-state case are obtained by omitting the term depending on Δt. Of course, a better rate of convergence with respect to Δt can be obtained is one uses a higher-order temporal discretization scheme and the exact solution is sufficiently smooth.

359 Using the method of manufactured solutions, we set the data in the differential equa-
360 tions, boundary conditions, and initial condition so that the exact solution of the SD
361 problem is given by

$$\begin{cases} u_c &= [x^2y^2 + e^{-y}]\cos(2\pi t) \\ v_c &= [-\frac{2}{3}xy^3 + [2 - \pi\sin(\pi x)]]\cos(2\pi t) \\ p_c &= -[2 - \pi\sin(\pi x)]\cos(2\pi y)\cos(2\pi t) \\ h_m &= [2 - \pi\sin(\pi x)][-y + \cos(\pi(1-y))]\cos(2\pi t). \end{cases}$$

362 We first consider a steady-state case for which the exact solution is chosen by setting
363 $t = 0$ in the above expressions. Table 4 gives the computationally derived convergence
364 rates as well as errors for this steady-state problem. We then consider the time-dependent
365 problem; based on the error estimate (18), we choose the time step to be related to the
366 spatial grid size by $\Delta t \sim h^3$ so that, according to that estimate, spatial and temporal
367 errors should be equilibrated. (A less onerous time step/spatial grid size relation would
368 be obtained if a higher-order temporal discretization is employed. For the purposes of
369 this paper, the discretization methods we use suffice.)

370 The resulting errors and rates of convergence are given in Table 5. The results in both
371 tables indicate that the finite element approximations converge at the optimal rate for the
372 discretization schemes used; in particular they are in agreement with the error estimate
373 (18).

374 In summary, as is the case for the CCPF model, we have used analytical and computa-
375 tional approaches to validate the SD model with the Beavers-Joseph interface condition
376 and to verify the correctness of the finite element codes we developed to obtain approxi-
377 mate solutions for that model.

3. Experimental Validation of Simulation Models

In Section 2, we provide mathematical and computational verifications that the finite element simulation codes we developed for solving the CCPF and SD models produce accurate results. For the SD system, we also use comparisons between the SD and Stokes-Brinkman models to validate the use of the Beavers-Joseph interface condition. What remains is to validate either or both models through comparisons with experimental results. Furthermore, both models contain a "tuning" parameter, i.e., α_{ccpf} in (5) and α_{sd} in (16). Thus, we also use experimental results to obtain some guidance about the value of these parameters. First, however, we describe the setup of the laboratory experiment.

3.1. Laboratory Setup

In Section 2, we used analytical and computational means for carrying out validation and verification studies of two models for karst aquifers, i.e., the CCPF and the SD (with the Beavers-Joseph interface condition) models. We now turn to using the results of laboratory experiments to further study the validity of the models. In this section, we provide a discussion of the experimental setup.

In *Faulkner et al.* [2009], a laboratory-analog experiment is used to simulate groundwater flow and solute transport in a karst aquifer with a single conduit buried adjacent to the matrix. The experiment mainly focused on water and solute exchange between the matrix and conduit. Here, we use the experimental results to benchmark and validate the computational models. For completeness, we briefly describe the experimental setup; details can be found in *Faulkner et al.* [2009].

Homogeneously packed glass beads are chosen to represent the matrix material. The bead dimensions are 30-40 US Sieve or 590-420 μm. A permeameter is fabricated to determine the conductivity of the glass beads matrix analog used in the experiment. Water

is allowed to flow into the unit with the dissolved air in the water removed. With the outlet tube at a fixed elevation and a constant head water supply to the permeameter, five outflow measurements are taken using a graduated cylinder and a stop watch. A Darcy-type experiment is used to measure the conductivity of the glass bead, which was found to be 0.0619 ± 0.0005 cm/s. The porosity of the beads was calculated to be 0.394, using the formula $n = V_v/V_t$, where n denotes the porosity (dimensionless), V_v the volume of void space, and V_t the total volume; see *Hornberger et al.* [1998].

A schematic figure of the principal components of the laboratory analog is shown in Figure 3 and the equipment laboratory setup is shown in Figure 4. The laboratory analog is constructed of transparent, acrylic plexiglas to allow digital imaging of the dye tracing experiments and provide support for instrumenting and confining the matrix of glass beads. The analog is divided into two domains. At the bottom is the conduit domain. The matrix domain occupies the rest of the space and has an inflow and outflow reservoir on either side. The inflow and outflow reservoirs and matrix material are separated from one another by stainless steel screens. The conduit is separated from the matrix domain by a stainless steel screen and plexiglas. The mesh size of the screen is slightly smaller than the size of the glass beads.

There are 28 ports available for measuring water inputs and outputs and hydraulic heads. The conduit has one inflow port and one outflow port as well as five ports for pressure transducers which are used for measuring hydraulic heads. The matrix domain has two inflow ports and two outflow ports. The matrix inflow and outflow reservoirs have one transducer port each and the main body of the matrix has fifteen transducer ports. Each domain has its own constant head water supply with the same components

as depicted in Figure 2. Tap water from a laboratory faucet is routed through inline water filters and flow meters at the inflow entrances. Water then flows into a module that contains a membrane that allows air entrained in the water to be removed by a vacuum pump as water flows through the device. This procedure reduces air bubbles that could form in the matrix which would significantly alter the hydraulic conductivity. The water is then routed through a float-style fill valve that maintains a constant head in each supply reservoir container. For imaging purposes, dye is added at the supply reservoir during an experiment.

The flow into each domain is measured by flow meters which are located downstream of the control valve just before the inflow ports of each domain. Water exiting the conduit flow meter is carried to the conduit port by vinyl tubing. Water exits the conduit via the conduit outflow port and/or enters the matrix domain through the stainless steel screen dividing the two domains. Water travels through the matrix and enters either the conduit through the screen dividing the two domains and/or enters the matrix outflow reservoir. Water exits the domain through two ports into vinyl tubes before entering a y-fitting that joins the two flows into one tube. The laboratory analog has a total of 22 ports available for communication with transducers. The information produced by the transducers and flow meters is retrieved and stored for analysis by the Laboratory Virtual Instrumentation Engineering Workbench (LabVIEW). Imaging is done using a digital camera whose operation, including settings and image capturing, is controlled by the GBTimelapse program from Granite Bay Software which is a Microsoft Windows application for the capture of time-lapse images.

The experiment is set up so that the head in the conduit is greater than the head in the matrix. This setting aims to simulate a flooding season. Several similar experimental cases for the flooding season were conducted; the results of a single experiment are chosen at random to be analyzed. Fluorescent red dye tracer is put into the conduit supply container, after the flow reaches a steady state, to visually trace water flow and aid in determining velocities. The LabVIEW program is started to record and convert analog voltage signals to actual pressures, flow rates, and volumes. The GBTimelapse program is initiated and captures images every ten seconds for the duration of the experiment. Hydraulic heads and flow rates from a screen shot captured at $t = 20$ seconds midway through the experiment are used in conjunction with transducer coordinates to generate actual total head pressure information. The total head distribution is contoured to allow a graphical visualization of pressures across the laboratory analog. Digital photos for the dye distributions are taken at every ten seconds as set by the GBTimelapse program.

3.2. Validation of Computer Simulation Models

We now compare experimental results to those obtained from computer simulations based on the CCPF and SD models. The model parameters used in the computer simulations are determined from the calibration of the experiment, e.g., the matrix porosity and hydraulic conductivity, or from the literature; see *Hua* [2009].

In *Bauer et al.* [2003]; *Birk et al.* [2003]; *Liedl et al.* [2003], it was concluded that the value of the exchange rate coefficient in the CCPF model α_{ccpf} should be proportional to the hydraulic conductivity K and also depend on the surface area available for the exchange of fluid between the matrix and conduit. Based on these observations and

calibrations of the matrix used in the experimental setup, a value of $\alpha_{ccpf} = 7.4\times10^{-4} m/s^2$ was chosen for simulations; see *Hua* [2009] for details.

For the parameter appearing in the Beavers-Joseph interface condition, we use the value $\alpha_{sd} = 0.2$ which is in the range suggested in *Beavers et al.* [1967].

Figure 5 shows the hydraulic head distribution obtained from the experiments and from computer simulations based on the SD and CCPF models. One observes that the SD simulation results are very close to the experimental results whereas the CCPF model generally overestimates the hydraulic heads in the matrix, especially at the boundary between the matrix and the conduit.

Figure 6 presents the experimental and computational results of tracer evolution (visualized using a dye in the experiments) at several time instants. The results of the SD simulation are very similar to the experimental results, but the CCPF simulation results are quite different. First, CCPF modeling underestimates dye-front movement in the conduit as well as the dye exchange at the interface between the conduit and matrix. Second, the modeling plume distribution in the matrix has a convex shape for the CCPF model and does not capture the characteristics of the plume distribution in the experiment, i.e., a broad U-shape with two humps caused by the two end points of the interface. The SD simulations does capture these features of the experimental results.

The results given in Figures 5 and 6 as well as other similar examples indicate that the SD model with the Beavers-Joseph interface condition is a valid model for coupled matrix-conduit flows and tracer transport. On the other hand, at least for the value of α_{ccpf} used in the calculations resulting in Figures 5 and 6, it seems that the CCPF model

is not validated. The question remains: can other values of α_{ccpf} yield better results? This question is addressed next.

4. Sensitivities of Modeling Parameters

Both the CCPF and SD models contain a modeling parameter, i.e., α_{ccpf} in (5) and α_{sd} in (16), respectively. In this section, we examine the sensitivity of solutions with respect to these parameters and also use experimental and computational results to gain some insight into the calibration of these parameters. A full study of the calibration of these parameters is ongoing work and will be reported in a forthcoming paper.

As is pointed out and verified in, e.g., *Bauer et al.* [2000, 2003]; *Birk et al.* [2003]; *Liedl et al.* [2003], the CCPF model is very sensitive to the value of exchange rate parameter α_{ccpf}. Those studies focused on the small values of the parameter, i.e., in the range of $O(1)$ multiples of the hydraulic conductivity. It was noted that as α_{ccpf} varies over this range, which is about zero to 10^{-3}, the breakthrough time of conduit genesis may vary over several orders of magnitude.

The high sensitivity of the CCPF model to changes in the exchange coefficient for small values of α may also be gleaned from an examination of the equation from which that sensitivity may be determined. For simplicity, we consider the steady-state case. Formal differentiation of the steady-state version of the equations in (6) with respect to α_{ccpf} yields the *sensitivity equations*

$$\begin{cases} -\nabla\cdot(K\nabla h'_m) + \alpha_{ccpf}(h'_m - h'_p)\delta_{\Omega_p} \\ \qquad\qquad = -(h_m - h_p)\delta_{\Omega_p} \ \text{ in } \Omega_m \\ -\dfrac{\partial}{\partial\tau}\Big(D\dfrac{\partial h'_p}{\partial\tau}\Big) - \alpha_{ccpf}(h'_m - h'_p) \\ \qquad\qquad = (h_m - h_p) \qquad \text{along } \Omega_p \end{cases} \tag{19}$$

for the sensitivities $h'_m = \partial h_m/\partial\alpha$ and $h'_p = \partial h_p/\partial\alpha$. Next, denote by $h_{m,0}$ and $h_{p,0}$ the solution of (6) for $\alpha_{ccpf} = 0$; note that in this case the equations in (6) for the conduit pipe Ω_p and matrix Ω_m uncouple. Then, from (19), we deduce that the sensitivities $h'_{m,0}$ and $h'_{p,0}$ evaluated at $\alpha_{ccpf} = 0$ are determined from

$$\begin{cases} -\nabla\cdot(K\nabla h'_{m,0}) = -(h_{m,0} - h_{p,0})\delta_{\Omega_p} & \text{in } \Omega_m \\ -\dfrac{\partial}{\partial\tau}\Big(D\dfrac{\partial h'_{p,0}}{\partial\tau}\Big) = (h_{m,0} - h_{p,0}) & \text{along } \Omega_p. \end{cases} \tag{20}$$

Now examine, for example, the first equation in (20); $(h_{m,0} - h_{p,0})$ is of $O(1)$ while K is of $O(10^{-4})$ so that $h'_{m,0}$ is of $O(10^4)$. Thus, we see that, h_m will change rapidly for small values of α_{ccpf}.

In general, quantities such as the exchange of fluid along the interface and the discharge in the conduit are sensitive to the choice of the value of the exchange parameter α_{ccpf}. In the laboratory experiment, the hydraulic conductivity of the glass beads is $6.19\times10^{-4}m/s$ so we set α_{ccpf} in the range of $[10^{-4}, 10^{-1}]$. Note that this is a range of *larger* values of α_{ccpf} than that used in the sensitivity studies in *Bauer et al.* [2000, 2003]; *Birk et al.* [2003]; *Liedl et al.* [2003]. We see from Figure 7 that the exchange flow rate at the matrix/conduit interface is very sensitive to the choice of α_{ccpf}. Note that for this study, we use discharge boundary condition at the inlet and outlet of the conduit pipe.

The SD model with the Beavers-Joseph interface condition seems to be much less sensitive with respect to its modeling parameter α_{sd}. In *Beavers et al.* [1967], it is suggested that α_{sd} should be chosen somewhere in the range $[0.2, 2]$. In Figure 8, we see that the exchange velocity and the conduit discharge for $\alpha_{sd} = 0.2$ and 2 are very nearly identical when the fixed inflow rate and out flow rate boundary conditions are specified for the

conduit. Thus, we see that the results of this model are not very sensitive to changes in α_{sd}.

In Section 3.2, we concluded that the SD model with the Beavers-Joseph interface condition produced results that were in good agreement with experimental results but that the CCPF model results were in not such good agreement for the parameter value $\alpha_{ccpf} = 7.4 \times 10^{-4} m/s^2$. We also just concluded that the SD model is largely insentive to the value of α_{sd}. Thus, to determine if other values of α_{ccpf} might yield better results when using the CCPF model, we compare results using that model with different values of α_{ccpf} to those obtained by using the SD model with $\alpha_{sd} = 0.2$. In Figure 9, such comparisons are provided for four values of α_{ccpf}. We see that agreement improves as the value of α_{ccpf} increases and that for the largest value, the agreement between the CCPF and SD results are quite good.

These results suggest the possibility that CCPF simulations of karst-like problems can be improved by using values for the exchange rate parameter α_{ccpf} that are larger than those that have been used in practice. Of course, a much more intensive study of this issue is needed before such a conclusion can be made definite. As mentioned above, this is a subject of our current work which involves applying optimization strategies to determine an optimal value for α_{ccpf} and for studying the dependence of the optimal value on other parameters defining the CCPF model.

5. Summary and Conclusions

In this paper, we have studied several issues related to two simulation models for flows in conduit/matrix systems. A summary of the paper is given as follows.

547 • In Section 2.1.1, we review the CCPF model for flows in conduit/matrix systems and
548 the results of mathematical analyses of the model.

549 • In Section 2.1.2, we validate a finite element CCPF simulation model using numerical
550 analyses and, using computational experiments, we verify the implementation codes for
551 the simulation model.

552 • In Section 2.2.1, we review the SD model for flows in conduit/matrix systems. In
553 particular, we discuss four choices used in the literature for the conditions that govern the
554 flow interchange at the conduit/matrix interface.

555 • In Section 2.2.2, we review, for the four choices for the interface conditions, the
556 results of a validation study in which asymptotic solutions for each choice are compared
557 to asymptotic solutions of the Stokes-Brinkman system. We concluding that the Beavers-
558 Joseph interface condition is the most accurate.

559 • In Section 2.2.3, we review mathematical and numerical analyses for the SD model
560 with the Beavers-Joseph interface condition and use those analyses to validate a finite
561 element SD simulation model. We also verify, using computational experiments, the
562 implementation codes for the simulation model.

563 • In Section 3.1, we discuss the laboratory setup for the experiments we perform to
564 provide data for further validation studies of the computer simulation models. These
565 studies suggest that the SD model with the Beavers-Joseph interface condition is a valid
566 model for conduit/matrix systems. On the other hand, perhaps the CCPF model with
567 the value of the exchange parameter chosen within the range suggested in the literature
568 does not result in good agreement with experimental observations. In particular, the
569 CCPF model overestimates the hydraulic heads along the interface between the matrix

and conduit, underestimate solute transport in the conduit, and does not capture well the plume distribution in the matrix.

• In Section 3.2, we examine the sensitivity of the CCPF model with respect to the exchange parameter, concluding that, as other authors have previously noted, that the model is highly sensitive for small values of the exchange parameter. However, for larger values, the model becomes less sensitive and, more important, also produces results that are in better agreement with experimental observations. This suggests that the CCPF model may also produce accurate simulation results, if one chooses larger values of the exchange parameter than those suggested in the literature. We also find that the SD model with the Beavers-Joseph interface is relatively insensitive to the value of the exchange parameter appearing in that model.

Acknowledgments. This work is supported by the CMG program of the National Science Foundation under grant numbers DMS-0620035 and DMS-0620091.

References

Barenblatt, G., I. Zheltov, and I. Kochina (1960), Basic concepts in the theory of seepage of homogeneous liquids in fissured rocks, *J. Appl. Math. Mech. (USSR), 24*, 1286–1303.

Bauer, S., R. Liedl, and M. Sauter, Modelling of karst development considering conduit-matrix exchange flow (2000), Calibration and reliability in groundwater modelling: coping with uncertainty, *IAHS Publ., 265*, 10–15.

Bauer, S., R. Liedl, and M. Sauter (2003), Modeling of karst aquifer genesis: Influence of exchange flow, *Water Resour. Res., 39*, 1285, doi:10.1029/2003WR002218.

Bear, J. (1972), *Dynamics of Fluids in Porous Media*, Dover.

591 Bear, J., and A. Verruijt (1987), *Modeling Groundwater Flow and Pollution*, D. Reidl,
592 Norwell, Mass.

593 Beavers, G., and D. Joseph (1967), Boundary conditions at a naturally permeable wall,
594 *J. Fluid Mech., 30*, 197–207.

595 Birk, S., R. Liedl, M. Sauter, and G. Teutsch (2003), Hydraulic boundary con-
596 ditions as a controlling factor in karst genesis, *Water Resour. Res., 39*, 1004,
597 doi:10.1029/2002WR001308.

598 Bobok, E. (1993), *Fluid Mechanics for Petroleum Engineers*, Elsevier, New York.

599 Brinkman, H. (1947), A calculation of the viscous force exerted by a flowing fluid on a
600 dense swarm of particles, *Appl. Sci. Res. A, 1*, 27–34.

601 Cao, Y., M. Gunzburger, F. Hua, and X. Wang (2009a), Coupled SD model with Beavers-
602 Joseph interface boundary condition, to appear in *Comm. Math. Sci.*.

603 Cao, Y., M. Gunzburger, B. Hu, F. Hua, X. Wang (2009b), and W. Zhao; Finite element
604 approximations for SD flow with Beaver-Joseph interface conditions; to appear in *SIAM*
605 *J. Numer. Anal.*

606 Cao, Y., M. Gunzburger, F. Hua, and X. Wang (2009c), Analysis and finite element
607 approximation of a coupled, continuum pipe-flow/Darcy model for flow in porous media
608 with embedded conduits; to appear in *Num. Meth. PDE.*

609 Cao, Y., H. Wang, and X. Xie (1988), Dual-media ow models of karst areas and their
610 application in north China, in *Karst Hydrogeology and Karst Environment Protection:*
611 *21st Congress of the International Association of Hydrogeologists*, Guilin, China, Int.
612 Assoc. of Hydrogeologists.

613 Chen Y., and J. Bian (1988), The media and movement of karst water, in *Karst Hydrogeol-*
614 *ogy and Karst Environment Protection: 21st Congress of the International Association*
615 *of Hydrogeologists*, Guilin, China, Int. Assoc. of Hydrogeologists.

616 Chen, N., M. Gunzburger, and X. Wang (2009), Asymptotic analysis of the differences
617 between the SD system with different interface conditions and the Stokes-Brinkman
618 system, preprint.

619 Clemens, T., D. Hŭckinghaus (1996), M. Sauter, R. Liedl, and G. Teutsch, A combined
620 continuum and discrete network reactive transport model for the simulation of karst
621 development, *IAHS Publ., 237*, 309–318.

622 Dershovitz, W., P. Wallmann, and S. Kindred (1991), Discrete fracture network modeling
623 for the Stripa site characterization and validation drift in flow predictions, *SKB Stripa*
624 *Technical Teport TR-91-16*, Swed. Nucl. Power and Waste Manage. Co., Stockholm.

625 Discacciati, M., E. Miglio, and A. Quarteroni (2002), Mathematical and numerical models
626 for coupling surface and groundwater flows, *Appl. Num. Math., 43*, 57–74.

627 Discacciati, M., and A. Quarteroni (2003), Analysis of a domain decomposition method
628 for the coupling of the Stokes and Darcy equations; in: F. Brezzi et al. (Eds.), *Numerical*
629 *Mathematics and Advanced Applications*, Springer, Milan, 3–20.

630 Discacciati, M., and A. Quarteroni (2004), Convergence analysis of a subdomain itera-
631 tive method for the finite element approximation of the coupling of Stokes and Darcy
632 equations; *Comput. Visual. Sci., 6*, 93–103.

633 Faulkner, J., B. Hu, S. Kish, and F. Hua (2009), Laboratory analog and numerical study
634 of groundwater flow and solute transport in a karst aquifer with conduit and matrix
635 domains, *J. Contam. Hydrol.*, in press.

636 Ford, D. (1998), Perspectives in karst hydrology and cavern genesis, *Bull. Hydrogeol., 16*,
637 9–29.

638 Ford, D., and P. Williams (1989), *Karst Geomorphology and Hydrology*, Chapman and
639 Hall, New York.

640 Gerke, H., and M. van Genuchten (1993a), A dual-porosity model for simulating the
641 preferential movement of water and solutes in structured porous media, *Water Resour.*
642 *Res., 29*, 305–319.

643 Gerke, H., and M. van Genuchten (1993b), Evaluation of a first-order water transfer term
644 for variably saturated dual-porosity models, *Water Resour. Res., 29*, 1225–1238.

645 Harbaugh, A. (2005), MODFLOW-2005, the U.S. geological survey modular ground-water
646 model – The ground-water flow process, *U.S. Geological Survey Techniques and Meth-*
647 *ods, 6*, A16.

648 Hornberger, G., J. Raffensperger, P. Wiberg, and K. Eshleman (1998), *Elements of Phys-*
649 *ical Hydrology*, John Hopkins University Press, Baltimore.

650 Hua, F. (2009), *Modeling, Analysis and Simulation of SD System with Beavers-Joseph*
651 *Interface Condition*, Ph.D. Thesis, Florida State University, Tallahassee.

652 Jäger, W., and A. Mikelić (2000), On the interface boundary condition of Beavers, Joseph
653 and Saffman, *SIAM J. Appl. Math., 60*, 1111–1127.

654 Jiang, B. (2009), A parallel domain decomposition method for coupling of surface and
655 groundwater flows, *Comput. Methods Appl. Mech. Engrg. ,198*, 947–957.

656 Jones, I. (1973), Reynolds number flow past a porous spherical shell, *Proc. Camb. Phil.*
657 *Soc., 73*, 231–238.

658 Katz, B., J. Catches, T. Bullen, and R. Michel (1998), Changes in the isotopic and
659 chemical composition of ground water resulting from a recharge pulse from a sinking
660 stream, *J. Hydrol., 211*, 178–207.

661 Kincaid, T. (2004), *Exploring the secrets of Wakulla Springs*, open seminar, Tallahassee.

662 Kiraly, L. (1998), Modeling karst aquifers by the combined discrete channel and continuum
663 approach, *Bull. Hydrogeol., 16*, 77–98.

664 Kuniansky, E., U.S. Geological Survey Karst Interest Group Proceedings, *U.S. Geological*
665 *Survey Scientific Investigations Report 2008-5023*, Bowling Green.

666 Layton, W., F. Schieweck, and I. Yotov (2003), Coupling fluid flow with porous media
667 flow, *SIAM J. Num. Anal., 40*, 2195–2218.

668 Le Bars, G., and M. Worster (2006), Interfacial conditions between a pure fluid and a
669 porous medium implications for binary alloy solidification, *J. Fluid Mech., 550*, 149–
670 173.

671 Li, G., D. Loper, and R. Kung (2008), Contaminant sequestration in karstic
672 aquifers: Experiments and quantification, *Water Resour. Res., 44*, W02429,
673 doi:10.1029/2006WR005797.

674 Liedl, R., M. Sauter, D. Hückinghaus, T. Clemens, and G. Teutsch (2003), Simulation of
675 the development of karst aquifers using a coupled continuum pipe flow model, *Water*
676 *Resour. Res., 39*, 1057, doi:10.1029/2001WR001206.

677 MacQuarrie, K., and E. Sudicky (1996), On the incorporation of drains into three-
678 dimensional variably saturated groundwater flow models, *Water Resour. Res., 32*, 447–
679 482.

680 Matusick, J., and P. Zanbergen (2007), Comparative study of groundwater vulnerability
681 in a karst aquifer in central Florida, *Geophy. Res. Abst., 9*, 04614.

682 McCabe, W., J. Smith, and P. Harriot (2005), *Unit Operations of Chemical Engineering*,
683 McGraw-Hill, New York.

684 Narasimhan, T. (1982), Multidimensional numerical simulaion of fluid flow in fractured
685 porous media, *Water Resour. Res., 18*, 1235–1247.

686 Neale, G. and W. Nader (1974), Prediction of transport processes within porous media:
687 Creeping flow relative to a fixed swarm of spherical particles, *AIChE J., 20*, 530–538.

688 Ochoa-Tapia, J. and S. Whitaker (1995), Momentum transfer at the boundary between a
689 porous medium and a homogeneous fluid: I-theoretical development, *Intl J. Heat Mass*
690 *Transfer, 38*, 2635–2646.

691 Sauter, M. (1992), *Quantication and forecasting of regional groundwater ow and trans-*
692 *port in a karst aquifer (Gal lusquel le, Malm SW Germany)*, Ph.D. Thesis, Univ. of
693 Tübingen, Tübinger, Germany.

694 Saffman, P. (1971), On the boundary condition at the interface of a porous medium, *Stud.*
695 *in Appl. Math., 1*, 77–84.

696 Shoemaker, W., E. Kuniansky, S. Birk, S. Bauer, and E. Swain (2008), Documentation of
697 a conduit flow process (CFP) for MODFLOW-2005, *U.S. Geological Survey Techniques*
698 *and Methods 6-A24*.

699 Taylor, C., and E. Greene (2001), Quantitative Approaches in Characterizing Karst
700 Aquifers: U.S. Geological Survey Karst Interest Group Proceedings, *Water Resources*
701 *Investigations Report 01-4011*, 164–166.

Teutsch, G. (1989), Two practical examples from the Swabian Alb, S. Germany, in *Proc. 4th Conference on Solving Groundwater Problems with Models*, Indianapolis, 1989.

Therrien, R., and E. Sudicky (1995), Three-dimensional analysis of variably-saturated flow and solute transport in discretely-fractured porous media, *J. of Cont. Hydrol., 23*, 1–44.

Worthington, S. (2003), A comprehensive strategy for understanding flow in a carbonate aquifer. in *Speleogenesis and Evolution of Karst Aquifers, 1*, 1–8.

h	$e_{p,0}$	$e_{m,0}$	$e_{p,1}$	$e_{m,1}$
2^{-2}	$3.05E$-1	$1.65E$-1	$3.87E$-0	$2.25E$-0
2^{-3}	$7.96E$-2	$4.24E$-2	$1.99E$-0	$1.16E$-0
2^{-4}	$2.01E$-2	$1.07E$-2	$1.01E$-0	$5.87E$-1
2^{-5}	$5.04E$-3	$2.68E$-3	$5.03E$-1	$2.94E$-1
2^{-6}	$1.26E$-3	$6.70E$-4	$2.52E$-1	$1.47E$-1
rate	1.981	1.987	0.987	0.985

Table 1. Errors and convergence rates of piecewise linear finite element approximations of solutions of the steady state CCPF mode; column headings correspond to $e_{p,0} = \|h_p - h_p^{fe}\|_0$, $e_{m,0} = \|h_m - h_m^{fe}\|_0$, $e_{p,1} = |h_p - h_p^{fe}|_1$, $e_{m,1} = |h_m - h_m^{fe}|_1$.

h	$e_{p,0}$	$e_{m,0}$	$e_{p,1}$	$e_{m,1}$
2^{-2}	$3.05E$-2	$1.64E$-2	$7.89E$-1	$6.91E$-2
2^{-3}	$3.91E$-3	$2.09E$-3	$2.02E$-1	$1.52E$-2
2^{-4}	$4.92E$-4	$2.63E$-4	$5.10E$-2	$3.58E$-3
2^{-5}	$6.15E$-5	$3.29E$-5	$1.28E$-2	$8.82E$-4
2^{-6}	$7.69E$-6	$4.11E$-6	$3.19E$-3	$2.20E$-4
rate	2.989	2.992	1.987	2.070

Table 2. Errors and convergence rates of piecewise quadratic finite element approximations of solutions of the steady state CCPF model; the column headings are as in Table 1.

	BJ	BJSJ	ZTCV	FS
conduit	ϵ^3/ν	ϵ^2/ν	ϵ/ν	$1/\nu$
matrix	ϵ^4/ν	ϵ^4/ν	ϵ^4/ν	ϵ^4/ν

Table 3. Comparison of the leading-order difference in the normal velocities for the Stokes-Brinkman model and the SD model with four choices of interface conditions.

h	$e_{\mathbf{u},0}$	$e_{\mathbf{u},1}$	$e_{p,0}$	$e_{h,0}$	$e_{h,1}$
2^{-3}	$2.83E$-4	$1.08E$-2	$8.57E$-3	$5.48E$-4	$3.12E$-2
2^{-4}	$3.63E$-5	$2.67E$-3	$1.93E$-3	$5.99E$-5	$7.78E$-3
2^{-5}	$4.61E$-6	$6.64E$-4	$4.65E$-4	$7.085E$-6	$1.94E$-3
2^{-6}	$5.80E$-7	$1.66E$-4	$1.15E$-4	$8.68E$-7	$4.86E$-4
rate	2.976	2.009	2.070	3.099	2.001

Table 4. Errors and convergence rates for the steady-state SD problem. Column headings correspond to $e_{\mathbf{u},0} = \|\mathbf{u}_c - \mathbf{u}_c^{fe}\|_0$, $e_{\mathbf{u},1} = |\mathbf{u} - \mathbf{u}^{fe}|_1$, $e_{p,0} = \|p_c - p_c^{fe}\|_0$, $e_{h,0} = \|h_m - h_m^{fe}\|_0$, $e_{h,1} = |h_m - h_m^{fe}|_1$.

h	$e_{\mathbf{u},0}$	$e_{\mathbf{u},1}$	$e_{p,0}$	$e_{h,0}$	$e_{h,1}$
2^{-3}	$1.11E$-3	$1.47E$-2	$1.56E$-2	$3.68E$-3	$4.31E$-2
2^{-4}	$1.43E$-4	$3.01E$-3	$2.18E$-3	$4.61E$-4	$9.26E$-3
2^{-5}	$1.80E$-5	$6.92E$-4	$4.30E$-4	$5.73E$-5	$2.12E$-3
2^{-6}	$2.25E$-6	$1.68E$-4	$1.06E$-4	$7.12E$-6	$5.08E$-4
rate	2.984	2.143	2.394	3.005	2.135

Table 5. Errors and convergence rates for the time dependent SD problem with $\Delta t \sim h^3$; the column headings are as in Table 4.

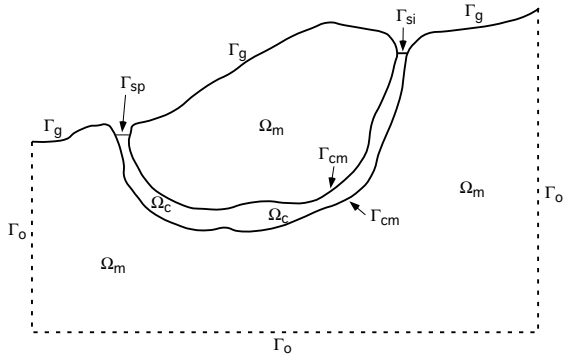

Figure 1. Conceptual model of a karst aquifer having a conduit Ω_c embedded in a matrix Ω_m.

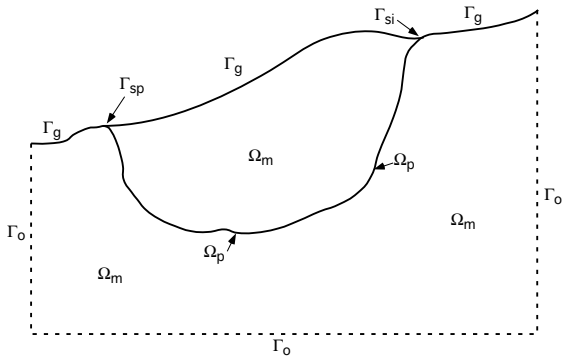

Figure 2. For the CCPF model, the conduit Ω_p in the conceptual model of a karst aquifer is a (one-dimensional) curve and the sinkhole and spring boundaries Γ_{si} and Γ_{sp} are the end points of the curve, respectively.

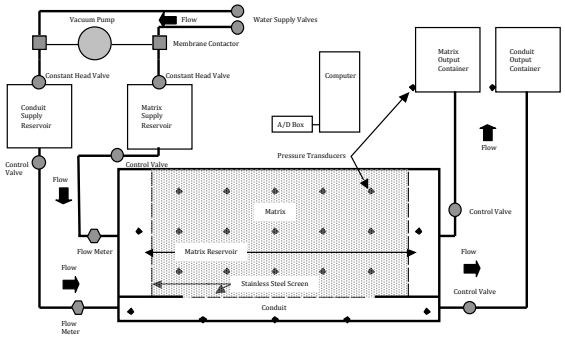

Figure 3. Schematic of the principal components of the laboratory analog.

Figure 4. Photograph of the laboratory setup.

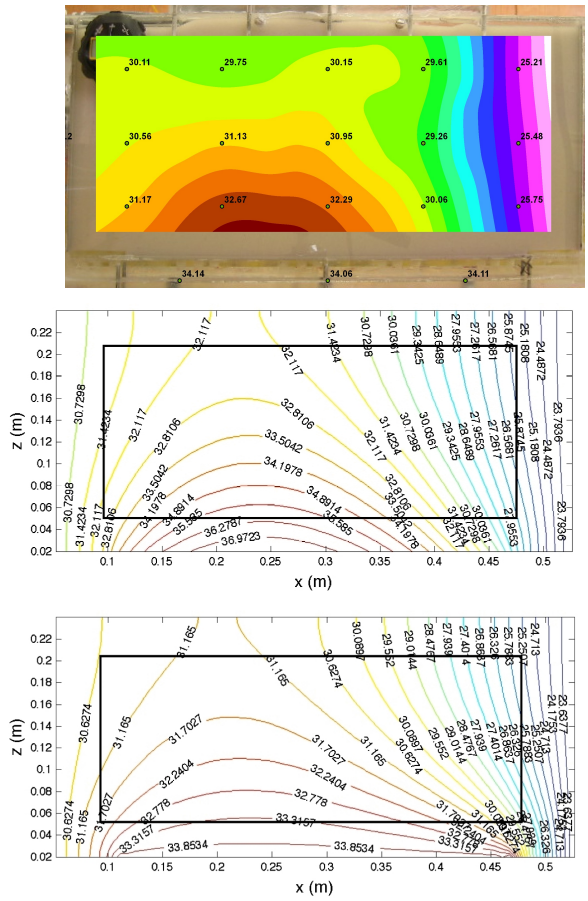

Figure 5. Experimental (top) and computational CCPF (middle) and SD (bottom) head distributions in the matrix.

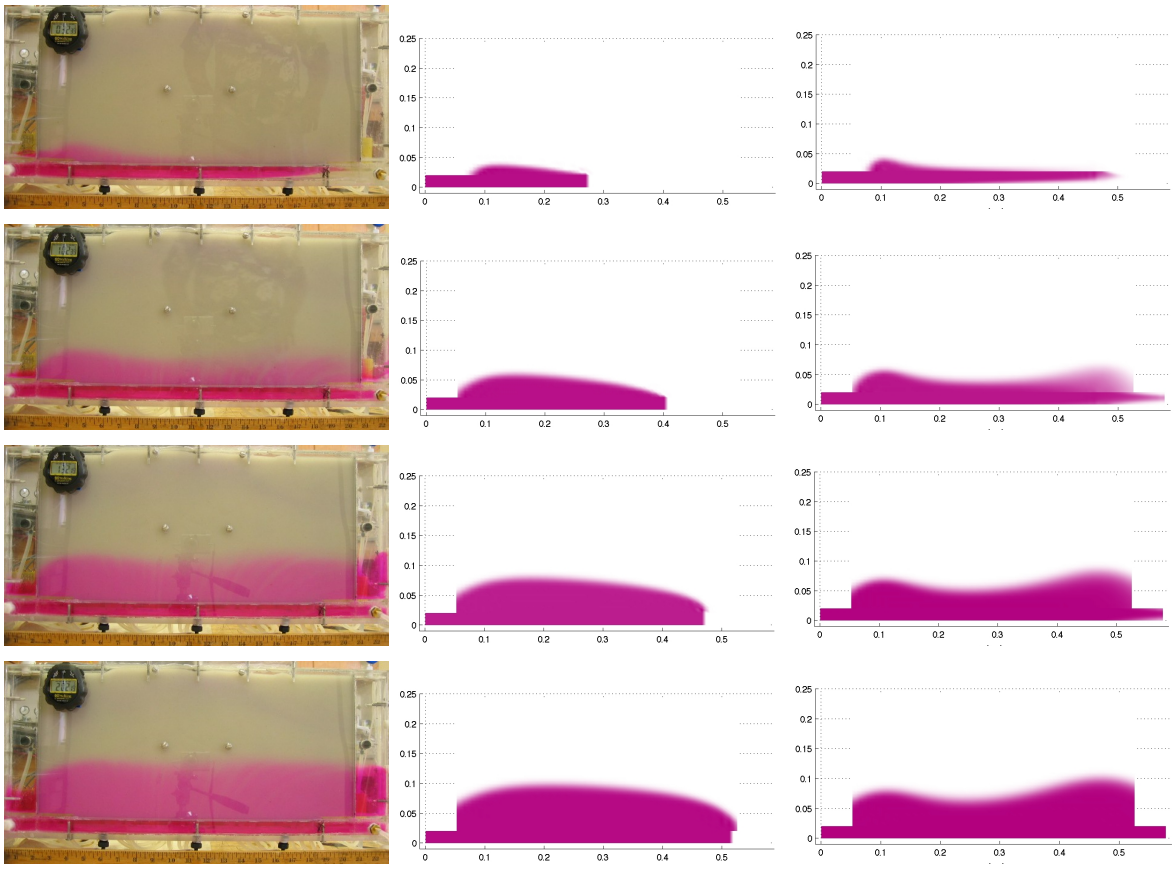

Figure 6. Experimental (left) and computational CCPF (middle) and SD (right) results for solute concentration in the matrix at times $t = 32.5s$, $62.5s$, $92.5s$, and $122.5s$.

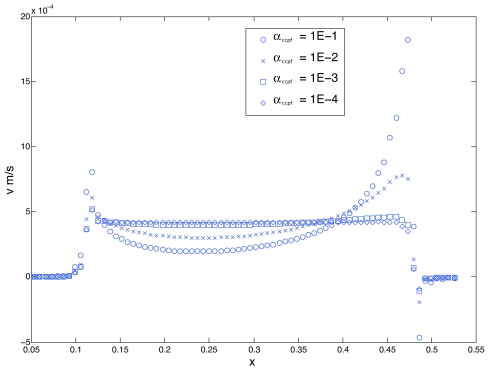

Figure 7. Normal velocity at the matrix/conduit interface for different values of the exchange rate coefficient α_{ccpf} in the CCPF model.

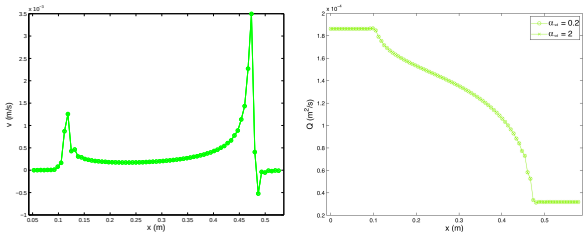

Figure 8. The exchange velocity (left) and conduit discharge (right) for different values obtained from SD simulations with $\alpha_{sd} = 0.2$ and 2.

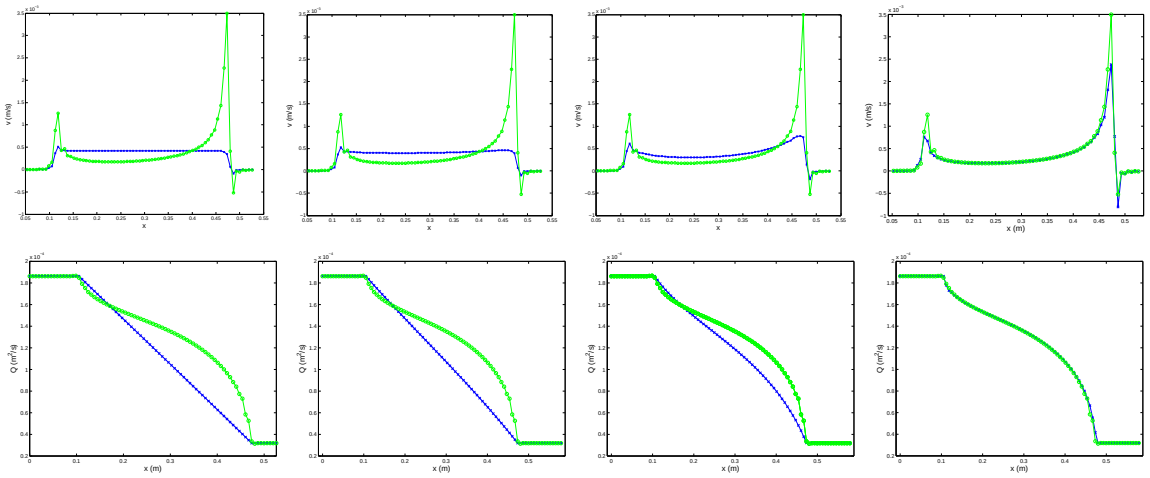

Figure 9. Comparison between SD (circles) and CCPF (hash marks) results for the exchange velocity (top) and conduit discharge (bottom) for different values of the exchange rate coefficient α_{ccpf} in the CCPF model; left to right: $\alpha_{ccpf} = 10^{-4}$, 10^{-3}, 10^{-2}, and 1.